ADVANCED MATERIALS
www.advmat.de

4D Printing of Freestanding Liquid Crystal Elastomers via Hybrid Additive Manufacturing

Xirui Peng, Shuai Wu, Xiaohao Sun, Liang Yue, S. Macrae Montgomery, Frédéric Demoly, Kun Zhou, Ruike Renee Zhao, and H. Jerry Qi**

Liquid crystal elastomers (LCE) are appealing candidates among active materials for 4D printing, due to their reversible, programmable and rapid actuation capabilities. Recent progress has been made on direct ink writing (DIW) or Digital Light Processing (DLP) to print LCEs with certain actuation. However, it remains a challenge to achieve complicated structures, such as spatial lattices with large actuation, due to the limitation of printing LCEs on the build platform or the previous layer. Herein, a novel method to 4D print freestanding LCEs on-the-fly by using laser-assisted DIW with an actuation strain up to −40% is proposed. This process is further hybridized with the DLP method for optional structural or removable supports to create active 3D architectures in a one-step additive process. Various objects, including hybrid active lattices, active tensegrity, an actuator with tunable stability, and 3D spatial LCE lattices, can be additively fabricated. The combination of DIW-printed functionally freestanding LCEs with the DLP-printed supporting structures thus provides new design freedom and fabrication capability for applications including soft robotics, smart structures, active metamaterials, and smart wearable devices.

1. Introduction

The recent decades have witnessed the booming of additive manufacturing (AM), or 3D printing, not only in conventional areas, such as aviation,[1] automobile[2] and construction,[3] but also in various emerging fields, such as electronics,[4] biomedical engineering[5] and soft robotics.[6] The reason is the growing capability of AM to fabricate complex structures, which are challenging to be realized by traditional machining methods. In this advancement, the material library of 3D printing is no longer limited to static materials for structural construction and has expanded to active materials or stimuli-responsive materials, such as shape memory polymers,[7] hydrogels,[8] magnetic soft materials[9] and liquid crystal elastomers (LCEs),[10] driven by the growing need for soft robots,[10h,11] biomedical devices,[5,8a] smart wearable devices,[12] etc. The active nature of stimuli-responsive materials adds the dimension of time to 3D printing and leads to the emerging 4D printing.[8a,13]

Among active materials for 4D printing, LCEs are appealing candidates due to their large, reversible and rapid actuation through a nematic–isotropic phase transition upon external stimuli, such as heat,[14] light,[10a,b,15] humidity[16] and electric fields.[17] LCEs are a class of soft active materials that inherit both the entropic elasticity of elastomers and the molecular anisotropy of liquid crystals (or mesogens). The actuation relies on the mesogen alignment,[18] which can be achieved by mechanical stretching,[19] surface shearing[10g] or external fields.[20]

3D/4D printing methods have been developed to fabricate LCE-based structures and align the mesogens. Direct ink writing (DIW) has been explored for printing LCEs.[11,15,21] In DIW, mesogens are aligned along the printing path when the LCE ink is extruded out of the syringe through the nozzle. Different inks have been developed for both high-temperature printing[10c,21a,c] and room-temperature printing.[21d,22] In addition, functionally graded LCEs were achieved by varying printing parameters,[10d,21c,g,23] such as printing temperature, printing speed and nozzle size. Although 3D structures, such as pinecone and saddle-shaped structures,[21c] can be achieved by 2D structures via different actuation strains between layers, the layer-by-layer manner of material deposition in DIW makes LCEs to be printed on the build platform or the previous layers.

X. Peng, X. Sun, L. Yue, S. M. Montgomery, H. J. Qi
The George W. Woodruff School of Mechanical Engineering
Georgia Institute of Technology
Atlanta, GA 30332, USA
E-mail: qih@me.gatech.edu
X. Peng, H. J. Qi
Renewable Bioproduct Institute
Georgia Institute of Technology
Atlanta, GA 30332, USA
S. Wu, R. R. Zhao
Department of Mechanical Engineering
Stanford University
Stanford, CA 94305, USA
E-mail: rrzhao@stanford.edu
F. Demoly
ICB UMR 6303 CNRS
Univ. Bourgogne Franche-Comté
UTBM
Belfort 90010, France
K. Zhou
Singapore Centre for 3D Printing
School of Mechanical and Aerospace Engineering
Nanyang Technological University
50 Nanyang Avenue, Singapore 639798, Singapore
The ORCID identification number(s) for the author(s) of this article can be found under https://doi.org/10.1002/adma.202204890.

DOI: 10.1002/adma.202204890

As a result, the actuation of the printed LCE structures is limited to planar shrinkage, simple bending, or twisting.

Recent progress has also been made in Digital Light Processing (DLP) printing of LCEs, where LCE inks are selectively cured by the light patterns from DLP projectors. A great advantage of this method is that the high resolution of selective photocuring enables the fabrication of fine lattices or structures with a higher level of complexity. Despite this advantage, aligning mesogens becomes a challenge. DLP-printed LCE lattices have been reported to show high energy-dissipation,[24] but the absence of actuation causes the method to fall short of the common expectations of using LCEs. More recently, the alignment of LCE mesogens was realized by the built-in shear separation mechanism of the DLP printer, and bending actuators were demonstrated.[10g] Still, this approach only aligns mesogens in one direction; hence, applications are limited to thin films and simple bending actuation.

In this study, we develop a novel hybrid additive manufacturing system that 4D prints freestanding LCE on-the-fly for 3D structures in a one-step additive process. This hybrid system consists of a top-down DLP and a DIW with an in situ laser-curing module. The laser curing module cures the LCE ink as it is extruded and stretched by the moving nozzle, while the DLP provides optional structural or removable supports. Unlike freestanding rigid materials such as metals,[25] rigid plastics,[26] fiber-reinforced thermoset composites[27] or glasses,[28] soft and flexible LCEs are difficult to print in the air while still retaining their shapes. Additionally, printing becomes more challenging when actuation capability is required to be kept for LCEs. To address this challenge, we rationally design the LCE ink and enable rapid curing upon extrusion to fix the shape and mesogen alignment. The stretching due to nozzle movement is further utilized to enhance mesogen alignment and thus actuation (up to −40% actuation strain). We also carefully choose the photoinitiator and laser wavelength for the LCE to avoid interference with the DLP inks. To the best of our knowledge, this is the first report of DIW printing of freestanding active materials on-the-fly. We further demonstrate that with this new capability, LCE-based active structures, such as hybrid lattices, active tensegrity, an actuator with tunable stability and 3D spatial lattices can be additively fabricated.

2. Results and Discussion

2.1. 4D Printing via DIW and DLP

To enable freestanding DIW printing of LCEs on-the-fly with DLP printing of optional structures, two challenges need to be overcome. First, the LCE ink should be cured rapidly upon extrusion. Second, the light used for curing LCEs should not polymerize the DLP inks. To address the first challenge, a laser-curable and room-temperature-printable LCE ink (**Figure 1**A) is formulated. In addition to the typical LCE inks that contain the diacrylate mesogens RM257 ((1,4-bis-[4-(3-acryloyloxypropyloxy) benzoyloxy]-2-methylbenzene), RM82 (1,4-bis-[4-(6-acryloyloxypropyloxy)benzoyloxy]-2-methylbenzene) and the dithiol flexible spacer EDDET ((2,2′-(ethylenedioxy)diethanethiol), a trifunctional acrylate-based crosslinker (pentaerythritol triacrylate [PETA]) is added for self-supporting and fast free-radical polymerization. To address the second challenge, we use a visible-light photoinitiator PI 784 ((bis(2,6-difluoro-3-(1-hydropyrrol-1-yl)phenyl)titanocene) to cure the LCE ink by lasers with a wavelength of 450 nm. As shown by the ultraviolet–visible (UV–Vis) characterization in Figure S1, Supporting Information, such specially selected photoinitiator and laser wavelength can effectively avoid unexpected curing of DLP inks, which use a UV-light photoinitiator PI 819 (phenylbis(2,4,6-trimethylbenzoyl)phosphine oxide) for photopolymerization, whose absorption ends near 450 nm. Also, the addition of the photoabsorber Sudan I into the DLP resins can further avoid unexpected curing by the laser, as this orange-red dye shows great light absorbance at 450 nm (Figure S1, Supporting Information). This rational design strategy is applied to all the optional DLP resins, including the rigid structural ink, the flexible structural ink and the soluble supporting ink.

As schematically depicted in Figure 1B, the optimized custom-built hybrid printing system[22] consists of two parts, namely, a laser-assisted DIW system and a DLP system (see Experimental Section for details). The build platform is mounted on a shared linear stage in the *z*-direction of the two systems. When the platform travels downward along the *z*-direction to the resin vat, the DLP projector irradiates the light pattern and selectively cures the resin layer-by-layer. When the platform is in the DIW position above the resin vat, the planar movement of the printing head in the *x*- and *y*-directions can be coordinated with the *z*-stage. The printing procedures are conducted by alternating the DIW and the DLP printing on demand. The LCE fibers are not limited to be printed in the *xy*-plane and can be inserted into DLP printing procedures as needed. For normal top–down DLP printing, there is always a thin layer of liquid resin on the top surface that remains uncured due to oxygen in the air, which inhibits free-radical polymerization.[29] This tacky surface shows poor adhesion to the LCE filaments[22] and makes the bonding extremely challenging when stretching is needed during LCE extrusion for better actuation. To overcome this issue, we purge oxygen by importing a protective gas (CO_2) to the resin vat so that the DLP printed parts can be fully cured and dried for better bonding with LCE filaments.

In the preparation of the LCE ink, the acrylate-terminated liquid crystal (LC, or mesogen) chains (Figure 1C) are first formed by a thiol-acrylate Michael addition reaction (Figure S2, Supporting Information). At this point, the oligomers exhibit a printable viscosity (Figure S3, Supporting Information). The mesogens can be aligned by shearing as being extruded through the nozzle and also by stretching due to the mismatch between the extrusion speed and the printing speed. Upon extrusion, the ink is immediately crosslinked by a laser module to fix the mesogen alignment. The laser module has four 450 nm lasers (Qiaoba 450 nm 5 mW blue dot laser diode, purchased from Amazon [Seattle, US]) to ensure unblocked irradiation of the extruded LCE ink. Because the laser is irradiated from the side with a tilted angle (≈45°), the effective irradiation area on the printing plane has an elliptical shape (Figure S4, Supporting Information). The four laser beams have an overlapping area of 4 mm diameter and provide a light intensity of ≈112 mW cm^{-2}. The printed LCE filament can be actuated to exhibit shrinkage along the printing direction upon heating.

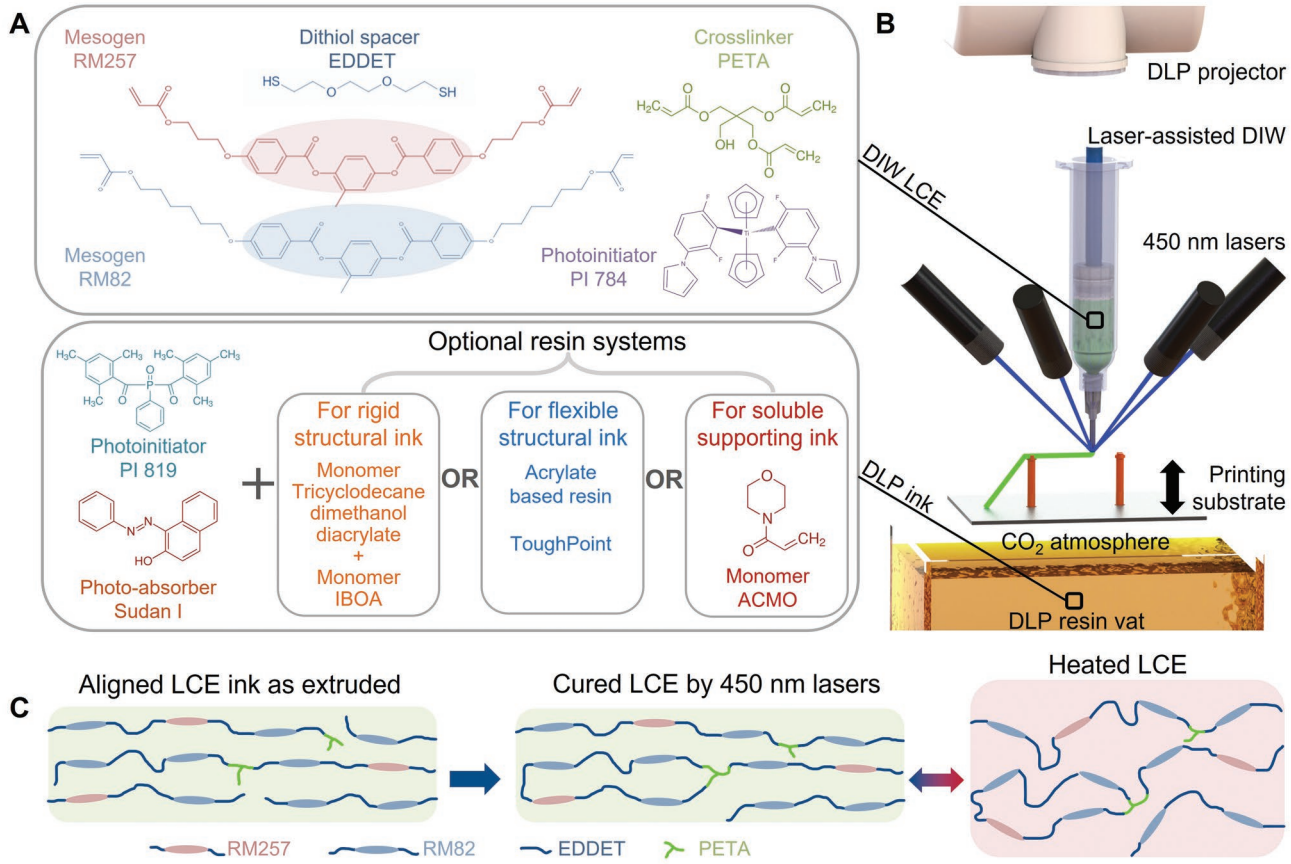

Figure 1. 4D printing of freestanding LCEs on-the-fly. A) Chemical structures of the LCE ink components and the components of optional DLP resin systems. The LCE ink consists of the mesogens (RM82 and RM257), dithiol spacer (EDDET), crosslinker (PETA), and photoinitiator (PI 784). Three resin systems are optional for DLP printing, including the rigid structural ink, the flexible structural ink and the soluble ink. All these three resins contain the photoinitiator (PI 819) and photoabsorber (Sudan I). B) Schematics of the laser-assisted hybrid DIW and DLP system. C) Evolution of the LCE ink during printing and actuation. Mesogens are aligned as extruded, and the aligned chains are crosslinked by 450 nm lasers. A reversible nematic–isotropic phase transition will occur upon heating, resulting in macroscopic shrinkage in the printing direction.

2.2. Dependence of LCE Properties on Printing Parameters

For freestanding LCE structures, the alignment of the mesogens is one of the most important properties concerning thermomechanical behaviors. As shown in **Figure 2**A, during printing, the alignment can be considered as a two-step procedure: first, the alignment is induced by shearing[11,15,21] as the ink is extruded out of the nozzle; and second, the alignment is further strengthened by stretching[19] due to the mismatch between the extrusion speed (v_e, determined by the printing pressure and the nozzle size) and nozzle moving speed (v_p, the printing speed). It should be noted that the selection of printing parameters concerning the speeds is also affecting the properties of the LCE, such as the filament diameter d, and curing status due to different effective curing times under different speeds. These properties of the LCE are important as they are related to the ability to stand freely against gravity, while the DLP materials are of less concern due to their greater stiffness.

To optimize the performance of the freestanding LCE, we study the relationship between the printing parameters and the properties of the printed LCE filaments, including the filament diameter, gel fraction and actuation. First, as an important physical dimension related to the stiffness of the freestanding structure, the diameter of the filaments printed by different nozzles is studied. As shown in Figure 2B, the static extrusion test (by keeping the nozzle static and extruding without stretching the filament) is conducted at 60 psi with different nozzles, namely, 22 Ga, 20 Ga, 18 Ga and 17 Ga, of which the inner diameters are 0.46, 0.64, 0.99 and 1.2 mm, respectively. All the nozzles are 12.7 mm in length. The measured diameters of the printed filaments are 0.59, 0.76, 1.34 and 1.42 mm, which are larger than the inner diameters of the nozzles because of the non-Newtonian-fluid nature of the ink. The viscosity of the ink is tested and shown in Figure S3, Supporting Information, showing shear thinning with the increasing shear rate. We then study the parameters related to the extrusion speed v_e. The ink is viscous but still printable at room temperature with a pressure booster (all pressure values are those supplied to the pressure booster, resulting in an intensified effective pressure to the syringe, which is four times the reported value). Figure 2C shows the effect of the nozzle size on the extrusion speed under a constant pressure applied (60 psi), demonstrating an inverse square relationship. Similarly, the extrusion speed can also be approximated as a linear function of the pressure

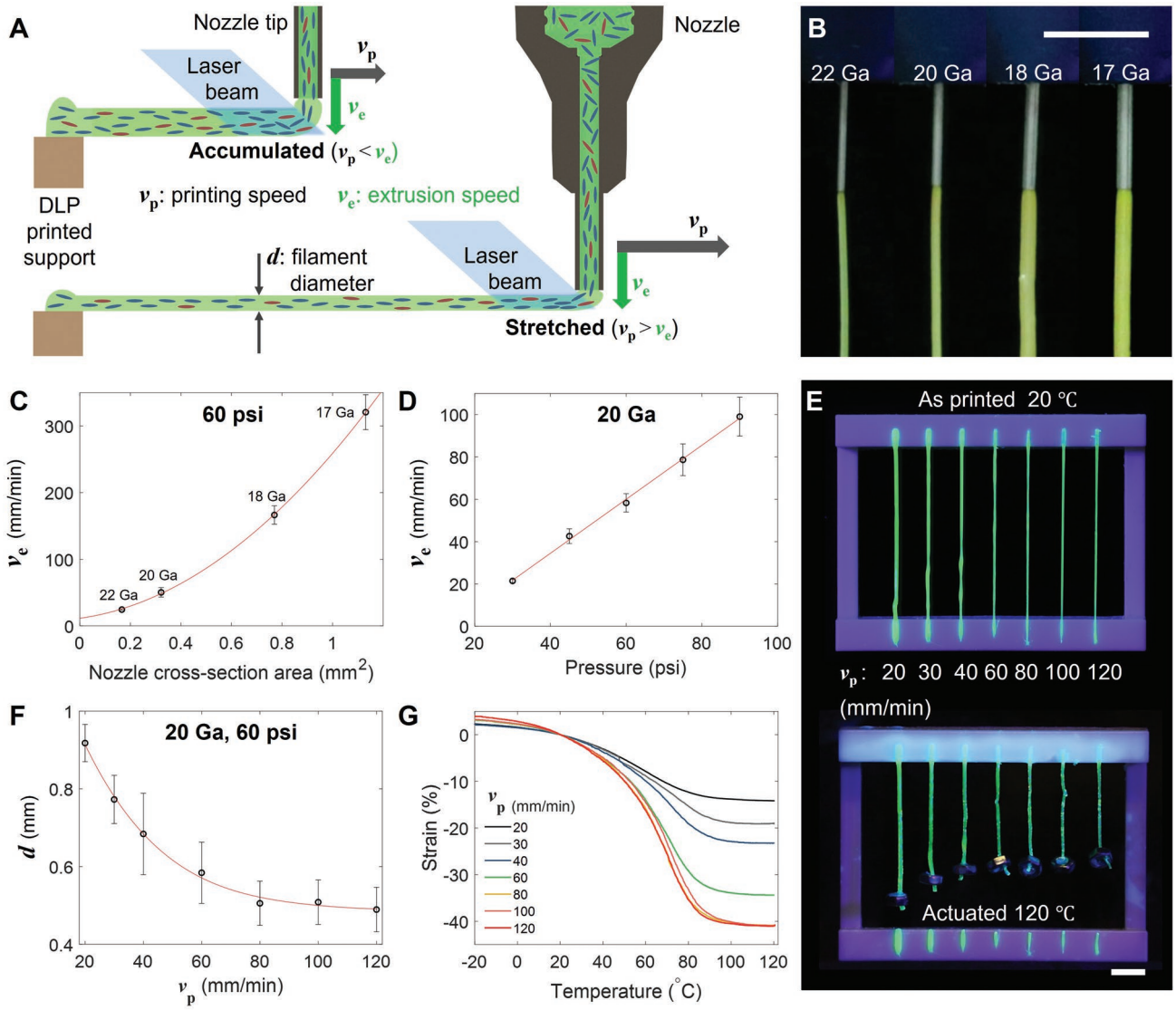

Figure 2. Characterizations of the LCE ink and printing parameters. A) Schematic illustration showing the effect of the mismatch between the extrusion speed (v_e) and the printing speed (v_p) during freestanding DIW printing of the LCE ink. B) LCE fibers extruded by nozzles of different sizes in the static condition at 60 psi. C) The relationship between the nozzle cross-section area and the extrusion speed under a constant pressure (60 psi, n = 4). D) The extrusion speed as a function of the pressure (with a nozzle of 20 Ga, n = 4). E) Freestanding LCE fibers printed at different speeds. The LCEs are printed on a frame with a span of 50 mm (top). For actuation, one end of each fiber is cut, and a mass of 0.3 g is attached. The fibers show graded actuation upon heating to 120 °C (bottom). F) The relationship between the printing speed and the fiber diameter d (20 Ga, 60 psi, error bars represent the diametral standard deviation of the fibers). G) The actuation test results of the freestanding LCE fibers with different printing speeds. Scale bars: 10 mm.

(Figure 2D). In general, the selection of the above parameters can be guided by the Hagen–Poiseuille law for an optimized extrusion speed.[30]

The effect of printing speed v_p to the actuation of the freestanding LCE fibers is then studied. As shown in Figure 2E and Movie S1, Supporting Information, seven freestanding LCE fibers are printed along a horizontal path on a frame with a span of 50 mm using the same nozzle (20 Ga) under the same pressure (60 psi) but at different printing speeds. Therefore, the degree of stretching during the printing is different. This difference in stretching not only causes the different filament diameters (as plotted with respect to the printing speed in Figure 2F) but also results in a different alignment and thus actuation. The assumption described above is further validated by the polarized optical microscope images (Figure S5, Supporting Information), which shows the increase of alignment with the increase of printing speed. To visually present the variation of actuation by the graded printing speed, the fibers are cut at the edge of the frame and attached with a nut (0.3 g). Upon heating to 120 °C in an oven, the fibers demonstrate different actuation strains corresponding to different printing speeds. Another group of fibers is printed to further quantify the actuation strain as a function of temperature, as shown in Figure 2G (more details of the actuation strain test

can be found in the Experimental Section). Here, the actuation strain is defined as ratio between the length change and the original length at 20 °C. The maximum actuation strain of different fibers increases with the printing speed from −14.2% at 20 mm min^{-1} and saturates at −40.1% strain at 80 mm min^{-1} (Figure S6, Supporting Information), indicating stretching can significantly enhance actuation. As demonstrated in the movies and actuation cycles as plotted in Figure S7, Supporting Information, the actuation of the freestanding LCE fibers are stably repeatable. Although faster printing speed generally results in better actuation, there is a trade-off in fiber strength as not only does the diameter decrease but also the effective curing time decreases. Therefore, the photocuring speed of the acrylate groups in the LCE ink sets the upper limit of the printing speed if the light intensity of the lasers is not increased. The side view (Figure S8, Supporting Information) of the as-printed fibers in Figure 2E shows that the fibers are strong enough to maintain the shape as the printing speed is below 120 mm min^{-1}, and the deflections of the freestanding fibers are small (<2.2 mm over a 50 mm span). The diameter variation along the printed fibers is also characterized and plotted in Figure S8, Supporting Information. To quantify the photocuring of the freestanding fibers under different speeds (20 Ga, 60 psi), the gel fraction (GF) of the fibers without further post-curing is tested and is plotted as in Figure S9, Supporting Information. At 20 mm min^{-1}, the GF measures 74% and it decreases to 45% as the printing speed increases to 120 mm min^{-1}. For the fibers fully cured after post-curing, the GF measures 89%. In the rest of the paper (except for the graded lattice printing), to ensure good printing quality and curing, the DIW printing is set at 60 mm min^{-1} (v_p) using 20 Ga nozzle at 60 psi pressure, which gives a GF of 55% and an actuation strain of −34.4%. The DLP printing is conducted at 5 s curing time per 50 μm layer for all the inks.

2.3. Active Lattices with Embedded LCE

The integration of freestanding LCEs with passive materials grants a new design space for creating active structures, as the unbounded LCE fibers enable various modes of actuation, which can greatly expand the functionalities of the printed active composites. To demonstrate this capability, we start with LCE-embedded lattices. **Figure 3**A shows the design of a cuboid lattice with three embedded LCE layers and the schematic illustrations of the printing procedure (also shown in Movie S2, Supporting Information). In Step 1, the first LCE layer is printed on the platform, which becomes freestanding when removed from the platform after printing. In Step 2, the first section of the pillars is printed by DLP, using the rigid structural ink (see Experimental Section for details of the ink). When the last DLP layer is cured before Step 3, CO_2 is imported to the resin vat (regulated at 1 psi), and the top surfaces of the pillars are fully cured and dried in 1 min (the same for all cases), providing strong adhesion to the LCE filaments. In Step 3, the LCE filaments are printed to connect the DLP pillars. For each LCE fiber, pre-extrusion with laser on is performed for 2 s to fix the LCE filament on the DLP pillar before the nozzle movement, and then the nozzle moves toward the ending point. The extrusion and laser curing are continued for 2 s upon arrival at the ending point. To finish, the nozzle moves quickly (150 mm s^{-1}) along the fiber orientation to break the filament. In Step 4, another half of the DLP pillars is printed, and the CO_2-assisted surface curing is conducted before Step 5. Finally, in Step 5, another layer of LCE filaments is printed in the same way as in Step 3. The printed lattice is washed with isopropyl alcohol and post-cured for 15 min under 380 nm UV light (all materials with either PI 819 or PI 784 can be further crosslinked by 380 nm UV light, see Figure S1, Supporting Information). To predict the actuation behaviors of the printed active composites, the finite element analysis (FEA) simulation is conducted (more details about FEA model can be found in the Supporting Information. See Figure S10, Supporting Information, for the nominal strain contour). As shown in Figure 3B, the experimental results match the simulation results well. The overall actuation strain of the lattice, measured in the *x*- and *y*- directions (as indicated in Figure 3B) is −23% and −29%, respectively. We can also replace part of the LCE filaments with DLP printed bridges, so that the actuation of the lattice in each direction can be tunable. Similarly, we design and print a circular lattice with two layers of LCE filaments (Figure 3C and Movie S3, Supporting Information). In each LCE layer, two concentric LCE circles are connected by the DLP bridges. Therefore, when the structure is heated, the distance between the LCE circles is not changing, but an obvious change in the total diameter (from 40 to 30.4 mm) of the lattice is demonstrated, which is well predicted by the FEA simulation.

2.4. Active Tensegrity and Actuator with Tunable Stability

In addition to the lattices with controllable shrinkage, we further demonstrate more functionality that can be achieved by this novel hybrid 3D printing method. Tensegrity is a class of structures consisting of compressive stiff struts and tensional strings. Although active tensegrity has been developed,[31] such structures need to be assembled due to the complexity of combining rigid and soft materials and the isolation of rigid struts with different orientations; it still remains a significant challenge to directly fabricate them by an AM approach. Enabled by the freestanding LCE printing capability, we can directly print active tensegrity with rigid rods and LCE strings without post-printing assembly. As shown in **Figure 4**A and Movie S4, Supporting Information, a layer of LCE strings is first printed on the platform. Then, the inclined rods are printed by the DLP rigid ink with Young's modulus of 1.8 GPa. This high stiffness helps the printing of the challenging unsupported inclining rod, which has a small slope (8 mm/40 mm). To ensure good bonding between the DLP rods and the glass platform, the ends of the rods are slightly enlarged, and the first three layers are cured for 25 s. At the end of the DLP printing process (the top surface of the rod), the CO_2 gas is imported to cover the resin vat so that a fully cured dry surface is ready for printing LCEs. Finally, the freestanding LCE strings are printed with 2 s of excessive extrusion time at the bonding points. This active tensegrity is relaxed under gravity when released from the printing platform. When it is heated, dramatic change in height (from 5.8 to 28 mm) is exhibited (Figure 4A and Movie S4, Supporting Information). The experimental procedures, including the relaxation under gravity, the actuation upon heating and the

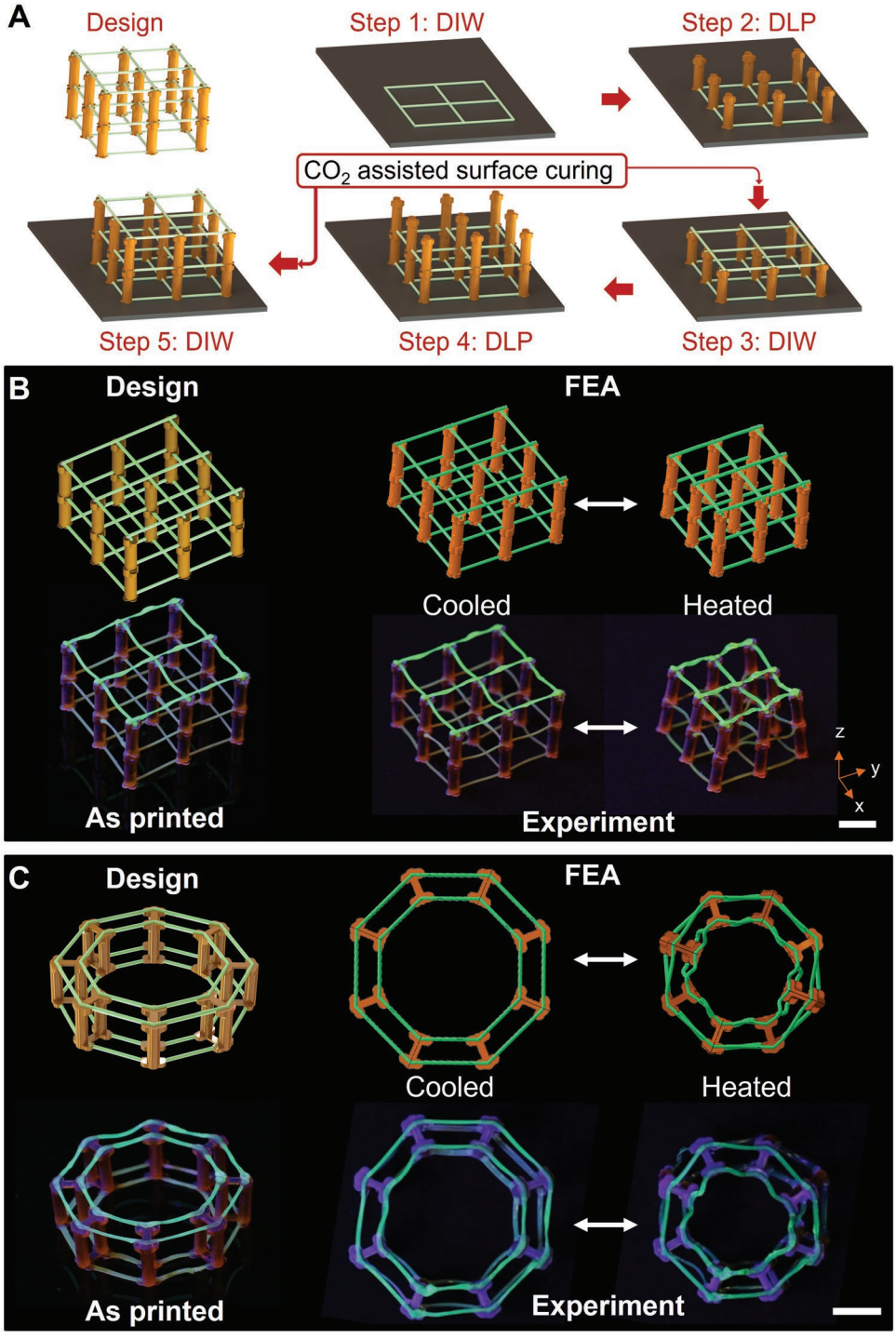

Figure 3. Hybrid printing of LCE-embedded active lattices. A) Schematic figures showing the printing procedure of a hybrid cuboid lattice with three independent freestanding LCE layers. Step 1: printing LCEs on the platform by DIW; Step 2: printing the first part of the pillars by DLP; before moving to the next step, CO_2-assisted surface curing is performed to obtain fully cured dry standing points for LCE fibers; Step 3: bridging the DLP printed pillars with freestanding LCEs by DIW; Step 4: continuing to finish the DLP pillars and cure the top surface with CO_2. Step 5: finishing DIW printing of freestanding LCEs. B) The design, finite element analysis (FEA) simulation result, printed part, and the experimental actuation of the hybrid cuboid lattice with the LCE embedded as shown in (A). C) The design, FEA simulation result, printed part, and the experimental actuation of the circular lattice. Scale bars: 10 mm.

recovery at cooling, are predicted by FEA simulation, and the results show a good match (Figure S11, Supporting Information, shows the nominal strain contour plots from simulations).

Furthermore, we create a hybrid printed actuator with tunable structural stability, as shown in Figure 4B. The actuator consists of a square main body with flexible hinges at the

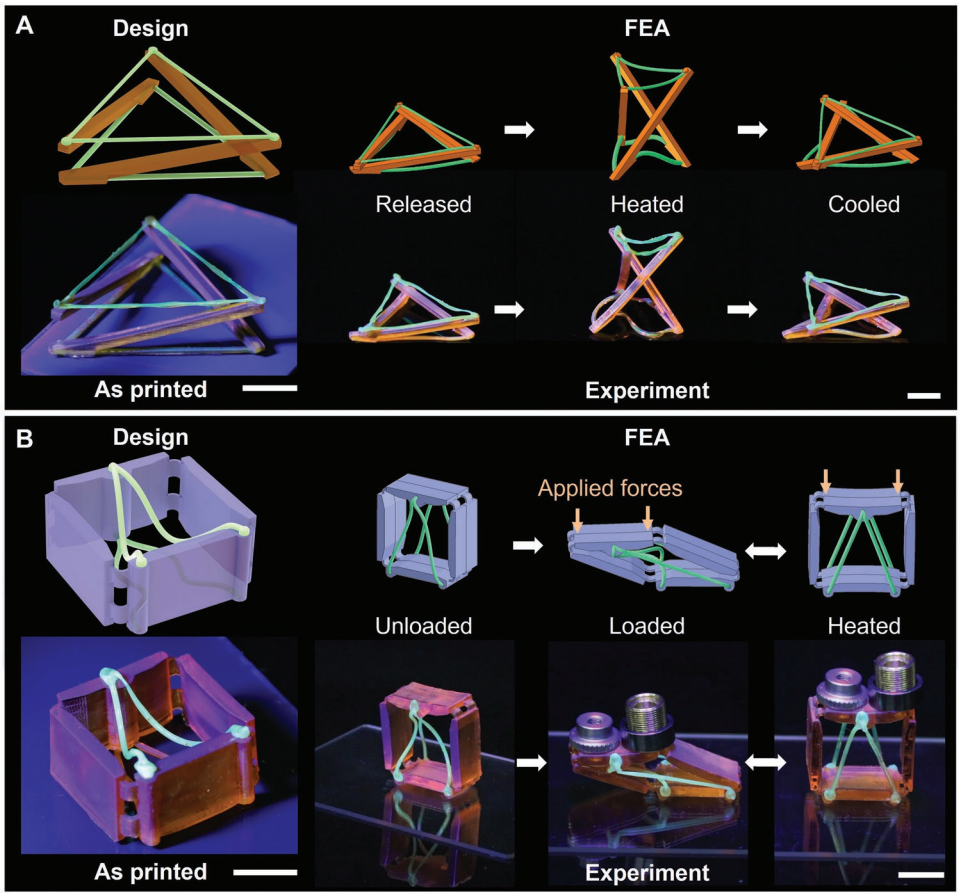

Figure 4. Hybrid printed active tensegrity and actuator. A) Hybrid printed active tensegrity with rigid DLP-printed rods and freestanding LCE strings. From left to right, shown are the design, FEA prediction of the collapsed status released from the printing platform under gravity, the actuated state with a dramatically increased height upon heating, and the relaxed state after cooling down. The printed structure and the experimental actuating process are shown below for comparison. B) Hybrid printed actuator with tunable structural stability. The redundant freestanding LCE fibers on the structure (printed by flexible structural ink) will not increase the stability of the structure until heated. The design and FEA prediction of the actuation are compared with the as-printed part and the experiment. Scale bars: 10 mm.

corners. Two groups of LCE fibers with excessive length are designed to connect the bottom corners to the top center of the main body. To print the relaxed LCE fibers with excessive length, we take the advantage of printing on-the-fly and write LCE fibers in 3D space. As shown in Movie S5, and Figure S12, Supporting Information, in DIW printing, the first point of the LCE is fixed on the platform through an excessive extrusion of 2 s. The DIW module then moves upward above the ending point with the pressure and laser on, so that the extruded filament length is longer than the distance between the starting and ending points. When the extrusion is finished, the DIW module stops extruding and laser curing and moves down in a detour to manipulate the orientation of the fiber on the platform. Finally, an excessive extrusion is conducted at the ending point to fix the other end of the fiber on the glass slide. The main body of the actuator is printed in a square shape by the DLP system with the flexible ink, and the top surface is also processed by CO_2-assisted curing before the last group of redundant LCE fibers is printed. Because of the soft corners used in the main body, it is not stable. The LCEs fibers, due to their excessive length, do not provide any force and thus the support to the structure at room temperature. Therefore, when the loads are placed on the top surface, the main body falls into a parallelogram shape. However, once the structure is heated, the LCE fibers are actuated and become short, thus imposing a tensile force to the structure and changing its stability. As shown in Figure 4B, the main body recovers to the square configuration upon heating and lifts the loads. The angle change is measured at 72°, while the height change is 14.6 mm (13.4 to 28 mm) during the actuation. It is worth noting that the weight of the structure is 2.359 g and the load is 6.733 g, while the LCE fibers only weigh 73.72 mg, giving a high load-to-weight ratio of 123. Similarly, FEA simulation is also conducted to predict the behavior of the actuator (nominal strain contour plots are provided in Figure S11, Supporting Information). More details of the FEA prediction can be found in the Supporting Information. As shown in these demonstrations, the integration of freestanding LCE printing with DLP opens a new way to fabricate architectures for applications such as soft robots and smart structures.

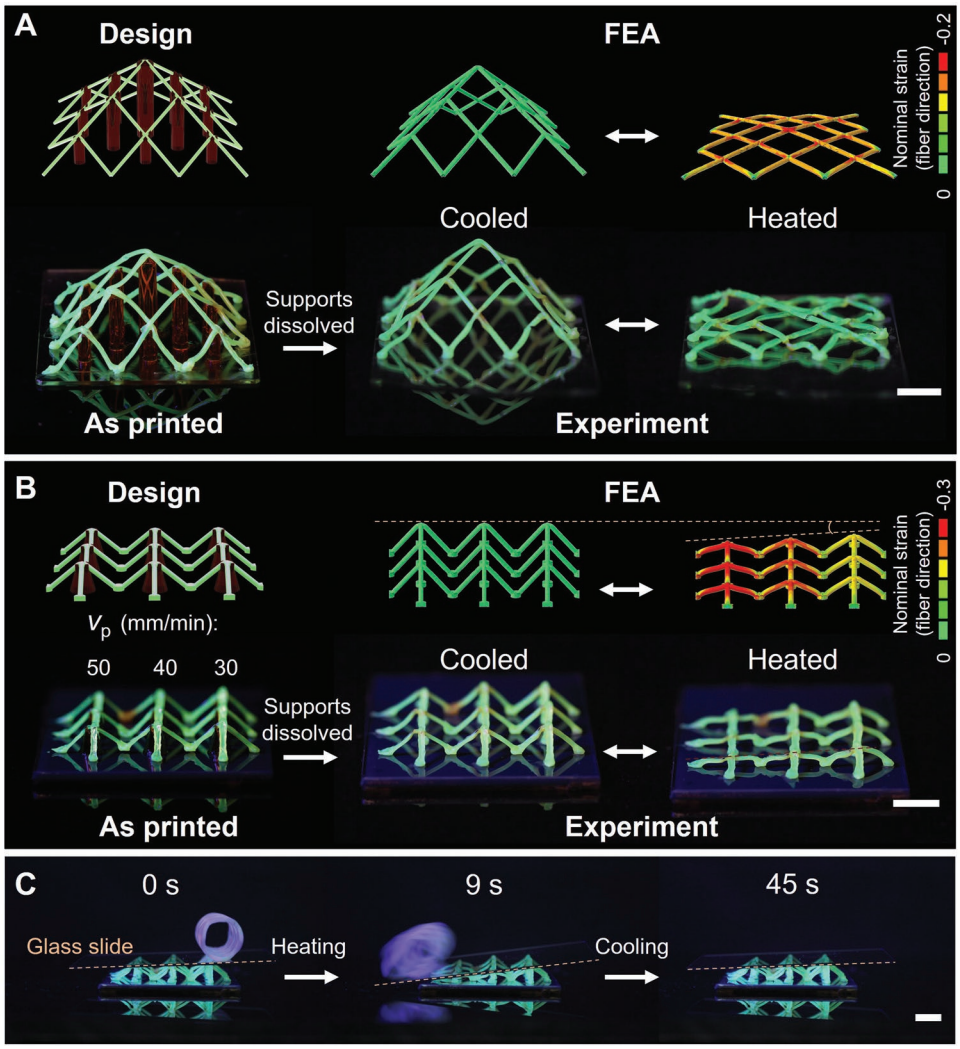

Figure 5. 3D spatial LCE lattices. A) The design and the printed structure of an LCE pyramid after dissolving the DLP-printed soluble supports, and the FEA prediction (color represents nominal strain along fiber direction) compared with experimental actuation of the LCE pyramid. B) A cellular LCE lattice with graded actuation enabled by different printing speeds (50, 40, and 30 mm min^{-1} from the left to the right column, respectively). Shown are the design, the printed architecture after dissolving the DLP printed supports, and the FEA simulation (color represents nominal strain along fiber direction) compared with the experimental actuation of the lattice. C) The application of the graded LCE lattice to launch the roller with a tilted surface upon heating. Scale bars: 10 mm.

2.5. 3D Spatial LCE Lattices

The hybrid printing method also enables the fabrication of the LCE lattice with soluble DLP-printed supports. The actuation of LCE filaments is hence no longer limited to planar shrinkage but can be programmed in a 3D space. To demonstrate this capability, an LCE pyramid is designed and printed, as shown in **Figure 5**A. Here, all the turning points of the LCE filaments are supported by the DLP printed pillars. Movie S6, Supporting Information, shows the printing process of this pyramid. First, the supporting pillars with different heights are printed using the removable supporting ink by DLP. Then, the LCE filaments are knitted by DIW on the top of the pillars. To fix the LCE filaments on the platform, excessive extrusion with laser on is performed for 2 s at the beginning and ending points. After printing, the whole architecture is washed by isopropyl alcohol and post-cured for 5 min under UV light (380 nm) to ensure that the LCE is fully crosslinked. Afterward, the supporting pillars are removed after being dissolved in water for 4 h, leaving the LCE pyramid only. The freestanding LCE pyramid can well support itself against gravity. Upon heating at 120 °C, the LCE pyramid collapses and the total height decreases from 23 to 6.83 mm (70.3% decrease in height). This collapsing actuation is successfully predicted by FEA simulation, as shown in Figure 5A. More details of the FEA prediction can be found in the Supporting Information.

As shown in Figure 2E,G, the printing speed can affect the actuation strain. We further harness this extra design space to fabricate the functionally graded LCEs. As shown in Figure 5B, a 3-by-3 cellular LCE lattice is designed and printed. In this cellular lattice, three columns of LCE cells are printed on the DLP supporting pillars with different printing speeds, namely, 50,

40 and 30 mm min^{-1}, from left to right, respectively. Excessive extrusion with laser on is also conducted for 2 s at the joints with the platform. All other printing parameters are kept the same as those with the pyramid. The supporting pillars are removed by dissolving them in water for 4 h. Upon heating at 120 °C, the lattice demonstrates graded actuation with respect to the printing speed, and the column on the left (50 mm min^{-1}) collapses the most (42.1% in height), while the column on the right shows the least deformation (17.1% in height). The graded actuation is successfully predicted by FEA, where three material models with different thermal expansion coefficient profiles are used. More details of FEA can be found in Supporting Information. As an application of this functionally graded LCE lattice, a roller launcher is demonstrated in Figure 5C and Movie S7, Supporting Information. A 50 mm × 75 mm × 1 mm glass slide is placed on top of the lattice, and the slide is horizontally leveled to hold a cylindrical roller at room temperature. However, once the LCE lattice is heated, the glass slide begins to incline. The angle of incline increases as the temperature increases. At 9 s from the beginning of heating, the roller rolls away. After 36 s of cooling in the air, the slide recovers to the horizontal position. The capability to print 3D spatial LCE lattices offers new opportunities for applications in active metamaterials and smart wearable devices.

3. Conclusion

We present a new approach for realizing 4D printing of freestanding LCE on-the-fly by the integration of laser-assisted DIW and DLP. To enable freestanding printing, an LCE ink is rationally developed for rapid curing. The actuation performance of printed LCE is further enhanced by stretching the ink by the movement of the printing nozzle to afford the actuation strain up to –40%. With three optional DLP resin systems, we further demonstrate various functionalities, including LCE-embedded active lattices, tensegrity, actuators with tunable stability and 3D spatial LCE. These demonstrations show that the combination of DIW-printed freestanding LCEs with the DLP-printed materials can provide new design freedom and fabrication capability for applications including soft robotics, smart structures, active metamaterials and smart wearable devices.

4. Experimental Section

Materials: 2-Methyl-1,4-phenylene bis(4-(3-(acryloyloxy)propoxy) benzoate) (RM257) and 2-methyl-1,4-phenylene bis(4-(6-(acryloyloxy) propoxy)benzoate) (RM82) were purchased from Wilshire Technologies (Princeton, NJ, USA). Bis(2,6-difluoro-3-(1-hydropyrrol-1-yl)phenyl) titanocene (PI 784) was purchased from Gelest Inc. (Morrisville, PA, USA). 2,2′-(Ethylenedioxy)diethanethiol (EDDET), pentaerythritol triacrylate (PETA), isobornyl acrylate (IBOA), tricyclodecane dimethanol diacrylate, catalyst triethylamine (TEA), radical inhibitor butylated hydroxytoluene (BHT), phenylbis(2,4,6-trimethylbenzoyl) phosphine oxide (PI 819), and Sudan I were purchased from Sigma-Aldrich (St. Louis, MO, USA). The fluorescent dye Solvent Green 5 was purchased from Orichem International Ltd. (Hangzhou, China). 4-Acryloylmorpholine (ACMO) was purchased from TCI American (Portland, OR, USA). ToughPoint (clear resin) was purchased from Adaptive3D (Dallas, TX, USA). All chemicals and materials were used as received without further purification.

Preparation of LCE Ink: To prepare the LCE ink, the method reported by Saed et al.[10c] was modified and optimized for preventing the ink from being cured by the ambient light during the ink-making procedures, and for assuring a proper room-temperature-printable ink viscosity can be yielded before usage. First, the LC diacrylates, RM82 and RM257 (RM82:RM257 weight ratio = 75:25) were mixed with the dithiol spacer EDDET and the crosslinker PETA. The molar ratio was 1.16:1:0.18 for thiol:LC acrylate:crosslinker acrylate. For better visualization, 0.01 wt% of fluorescent dye Solvent Green 5 was also added. The mixture was melted at 80 °C, and mixed with 0.6 wt% of PI 784, 2.5 wt% of BHT, and 0.6 wt% of TEA. Finally, the mixture was transferred to a 10 cc UV-blocking syringe and put in the oven at 65 °C for 3 h for oligomerization. The ink was stored at –18 °C before usage, and was recovered to room temperature (20–25 °C) during printing. The differential scanning calorimetry characterizations of the LCE ink and cured LCE are shown in Figure S13, Supporting Information, and the dynamic mechanical analysis characterization of the cured LCE is plotted in Figure S14, Supporting Information.

Preparation of DLP Inks: A previously reported resin[32] was used as the rigid structural ink. IBOA and tricyclodecane dimethanol diacrylate were mixed with a weight ratio of 80:20. 0.8 wt% of the PI 819 and 0.04 wt% of Sudan I were also added. A 50 µm layer was cured for 5 s. The cured resin showed a good linear elastic behavior with a high Young's modulus of 1.8 GPa.[32]

Commercially available acrylate-thiol photopolymer resin ToughPoint was adopted. In addition, 0.07 wt% of Sudan I and 0.8 wt% of PI 819 were also added for optimal DLP printability. A 50 µm layer was also cured for 5 s. The cured material was tough at room temperature but becomes flexible when it was heated up (T_g = 44 °C, dynamic mechanical analysis characterization plotted in Figure S14, Supporting Information).

A single-monomer ink with ACMO was used as the soluble supporting ink. 0.5 wt% of PI 819 and 0.07 wt% of Sudan I were added as the photoinitiator and photo absorber, respectively. The low viscosity of the ink ensured the ease of DLP printing. A 50 µm layer of ink could be photopolymerized (Figure S15, Supporting Information) in 5 s.

Hybrid 3D Printing: The assemblies consisting of both DLP and DIW parts were first designed in SOLIDWORKS (Dassault Systèmes, Velizy-Villacoublay, France) and then exported as STL files for further processing. The STL files for the DLP parts were sliced by the CreationWorkshop software (DaraTree3D, Dallas, TX, USA) to generate the PNG figures for the DLP projector. The G-codes for DIW printing were generated by the custom printing control program according to a model-option-input file, where the customizable printing options, such as the coordinates of the starting point, turning points, ending point, pre/post-extrusion time and printing speed were specified. The general printing method was reported in the previous work,[22] and more details of the setup for freestanding LCE printing are provided in the Supporting Information and Figure S16, Supporting Information.

Actuation Measurement: The actuation of the LCE samples was measured on the dynamic mechanical analyzer using the controlled force (1 mN preload) method. Sample fibers (20 mm in length) were first heated to 120 °C and stabilized for 10 min. Then, a temperature ramp of –5 °C min^{-1} was applied to cool the sample down to –20 °C. More details can be found in the Supporting Information.

Statistical Analysis: Error bars in the plots indicate the standard deviation over at least four tests on the specimens. All data were processed using MATLAB.

Supporting Information

Supporting Information is available from the Wiley Online Library or from the author.

Acknowledgements

X.P. and S.W. contributed equally to this work. H.J.Q. acknowledges the support from an AFOSR grant (FA 9550-20-1-0306; B.-L. "Les"

Lee, Program Manager), the gift funds from HP Inc. and Northrop Grumman Corporation. R.R.Z. and S.W. acknowledge the support of NSF Career Award CMMI-2145601 and NSF Award CMMI-2142789. X.P. acknowledges the partial support form Xerox Corporation. The authors also acknowledge the Open Polymer Active Learning Laboratory (OPALL) and Zhaoxian Zhang at Georgia Tech for their assistance with microscope imaging. This work is performed in part at the Georgia Tech Institute for Electronics and Nanotechnology, a member of the National Nanotechnology Coordinated Infrastructure, which is supported by the National Science Foundation (ECCS-1542174).

Conflict of Interest

The authors declare no conflict of interest.

Data Availability Statement

The data that support the findings of this study are available from the corresponding author upon reasonable request.

Keywords

4D printing, hybrid 3D printing, liquid crystal elastomers, multimaterial 3D printing, soft robots

Received: May 30, 2022
Revised: July 25, 2022
Published online: August 29, 2022

[1] a) A. Gisario, M. Kazarian, F. Martina, M. Mehrpouya, *J. Manuf. Syst.* **2019**, *53*, 124; b) J. C. Najmon, S. Raeisi, A. Tovar, in *Additive Manufacturing for the Aerospace Industry*, (Eds: F. Froes, R. Boyer), Elsevier, **2019**, p. 7.

[2] a) D. Gu, X. Shi, R. Poprawe, D. L. Bourell, R. Setchi, J. Zhu, *Science* **2021**, *372*, eabg1487; b) M. Wiese, S. Thiede, C. Herrmann, *Addit. Manuf.* **2020**, *36*, 101582.

[3] a) Y. W. D. Tay, B. Panda, S. C. Paul, N. A. Noor Mohamed, M. J. Tan, K. F. Leong, *Virtual Phys. Prototyping* **2017**, *12*, 261; b) A. Paolini, S. Kollmannsberger, E. Rank, *Addit. Manuf.* **2019**, *30*, 100894.

[4] a) A. D. Valentine, T. A. Busbee, J. W. Boley, J. R. Raney, A. Chortos, A. Kotikian, J. D. Berrigan, M. F. Durstock, J. A. Lewis, *Adv. Mater.* **2017**, *29*, 1703817; b) D. J. Roach, C. M. Hamel, C. K. Dunn, M. V. Johnson, X. Kuang, H. J. Qi, *Addit. Manuf.* **2019**, *29*, 100819.

[5] a) S. Singh, S. Ramakrishna, *Curr. Opin. Biomed. Eng.* **2017**, *2*, 105; b) S. V. Murphy, A. Atala, *Nat. Biotechnol.* **2014**, *32*, 773.

[6] a) N. W. Bartlett, M. T. Tolley, J. T. Overvelde, J. C. Weaver, B. Mosadegh, K. Bertoldi, G. M. Whitesides, R. J. Wood, *Science* **2015**, *349*, 161; b) J. Z. Gul, M. Sajid, M. M. Rehman, G. U. Siddiqui, I. Shah, K.-H. Kim, J.-W. Lee, K. H. Choi, *Sci. Technol. Adv. Mater.* **2018**, *19*, 243.

[7] a) Q. Ge, H. J. Qi, M. L. Dunn, *Appl. Phys. Lett.* **2013**, *103*, 131901; b) Q. Ge, C. K. Dunn, H. J. Qi, M. L. Dunn, *Smart Mater. Struct.* **2014**, *23*, 094007; c) Q. Ge, A. H. Sakhaei, H. Lee, C. K. Dunn, N. X. Fang, M. L. Dunn, *Sci. Rep.* **2016**, *6*, 31110; d) X. Kuang, K. Chen, C. K. Dunn, J. Wu, V. C. Li, H. J. Qi, *ACS Appl. Mater. Interfaces* **2018**, *10*, 7381.

[8] a) A. S. Gladman, E. A. Matsumoto, R. G. Nuzzo, L. Mahadevan, J. A. Lewis, *Nat. Mater.* **2016**, *15*, 413; b) F. G. Downs, D. J. Lunn, M. J. Booth, J. B. Sauer, W. J. Ramsay, R. G. Klemperer, C. J. Hawker, H. Bayley, *Nat. Chem.* **2020**, *12*, 363; c) M. Lei, W. Hong, Z. Zhao, C. Hamel, M. Chen, H. Lu, H. J. Qi, *ACS Appl. Mater. Interfaces* **2019**, *11*, 22768.

[9] a) C. P. Ma, S. Wu, Q. J. Ze, X. Kuang, R. D. Zhang, H. J. Qi, R. K. Zhao, *ACS Appl. Mater. Interfaces* **2021**, *13*, 12639; b) S. Wu, C. M. Hamel, Q. Ze, F. Yang, H. J. Qi, R. Zhao, *Adv. Intell. Syst.* **2020**, *2*, 2000060.

[10] a) H. Zeng, P. Wasylczyk, C. Parmeggiani, D. Martella, M. Burresi, D. S. Wiersma, *Adv. Mater.* **2015**, *27*, 3883; b) C. Yuan, D. J. Roach, C. K. Dunn, Q. Mu, X. Kuang, C. M. Yakacki, T. J. Wang, K. Yu, H. J. Qi, *Soft Matter* **2017**, *13*, 5558; c) M. O. Saed, C. P. Ambulo, H. Kim, R. De, V. Raval, K. Searles, D. A. Siddiqui, J. M. O. Cue, M. C. Stefan, M. R. Shankar, T. H. Ware, *Adv. Funct. Mater.* **2018**, *29*, 1806412; d) Z. Wang, Z. Wang, Y. Zheng, Q. He, Y. Wang, S. Cai, *Sci. Adv.* **2020**, *6*, eabc0034; e) M. Del Pozo, J. A. H. P. Sol, A. P. H. J. Schenning, M. G. Debije, *Adv. Mater.* **2021**, *34*, 2104390; f) J. H. Lee, J. Bae, J. H. Hwang, M. Y. Choi, Y. S. Kim, S. Park, J. H. Na, D. G. Kim, S. k. Ahn, *Adv. Funct. Mater.* **2021**, *32*, 2110360; g) S. Li, H. Bai, Z. Liu, X. Zhang, C. Huang, L. W. Wiesner, M. Silberstein, R. F. Shepherd, *Sci. Adv.* **2021**, *7*, eabg3677; h) C. Yuan, D. J. Roach, C. K. Dunn, Q. Mu, X. Kuang, C. M. Yakacki, T. Wang, K. Yu, H. J. Qi, *Soft Matter* **2017**, *13*, 5558; i) D. J. Roach, X. Kuang, C. Yuan, K. Chen, H. J. Qi, *Smart Mater. Struct.* **2018**, *27*, 125011.

[11] M. Lopez-Valdeolivas, D. Q. Liu, D. J. Broer, C. Sanchez-Somolinos, *Macromol. Rapid Commun.* **2018**, *39*, 1700710.

[12] a) S. Xu, Y. Zhang, L. Jia, K. E. Mathewson, K.-I. Jang, J. Kim, H. Fu, X. Huang, P. Chava, R. Wang, *Science* **2014**, *344*, 70; b) W. Gao, S. Emaminejad, H. Y. Y. Nyein, S. Challa, K. Chen, A. Peck, H. M. Fahad, H. Ota, H. Shiraki, D. Kiriya, *Nature* **2016**, *529*, 509; c) T. Cheng, M. Thielen, S. Poppinga, Y. Tahouni, D. Wood, T. Steinberg, A. Menges, T. Speck, *Adv. Sci.* **2021**, *8*, 2100411.

[13] a) Z. Ding, C. Yuan, X. Peng, T. Wang, H. J. Qi, M. L. Dunn, *Sci. Adv.* **2017**, *3*, e1602890; b) T. Le, S. Etigowni, S. Liang, X. Peng, J. Qi, M. Javanmard, S. Zonouz, R. Beyah, in *Annu. Computer Security Applications Conf.*, Association for Computing Machinery, New York **2021**, pp. 732–747; c) X. Sun, L. Yue, L. Yu, H. Shao, X. Peng, K. Zhou, F. Demoly, R. Zhao, H. J. Qi, *Adv. Funct. Mater.* **2021**, *32*, 2109805; d) X. Kuang, D. J. Roach, J. Wu, C. M. Hamel, Z. Ding, T. Wang, M. L. Dunn, H. J. Qi, *Adv. Funct. Mater.* **2019**, *29*, 1805290.

[14] a) J. Wu, S. Yao, H. Zhang, W. Man, Z. Bai, F. Zhang, X. Wang, D. Fang, Y. Zhang, *Adv. Mater.* **2021**, *33*, 2106175; b) Y. Wu, Y. Yang, X. Qian, Q. Chen, Y. Wei, Y. Ji, *Angew. Chem., Int. Ed.* **2020**, *59*, 4778.

[15] E. C. Davidson, A. Kotikian, S. C. Li, J. Aizenberg, J. A. Lewis, *Adv. Mater.* **2020**, *32*, 1905682.

[16] J. A. Sol, L. G. Smits, A. P. H. J. Schenning, M. G. Debije, *Adv. Funct. Mater.* **2022**, *32*, 2201766.

[17] P.-G. De Gennes, J. Prost, *The Physics of Liquid Crystals*, Oxford University Press, Oxford, UK **1993**.

[18] J. Zhao, L. Zhang, J. Hu, *Adv. Intell. Syst.* **2022**, *4*, 2100065.

[19] C. M. Yakacki, M. Saed, D. P. Nair, T. Gong, S. M. Reed, C. N. Bowman, *RSC Adv.* **2015**, *5*, 18997.

[20] a) S. Garoff, R. B. Meyer, *Phys. Rev. A* **1979**, *19*, 338; b) Z. Li, G. A. Di Lisi, R. G. Petschek, C. Rosenblatt, *Phys. Rev. A* **1990**, *41*, 1997; c) J. Shin, M. Kang, T. Tsai, C. Leal, P. V. Braun, D. G. Cahill, *ACS Macro Lett.* **2016**, *5*, 955.

[21] a) C. P. Ambulo, J. J. Burroughs, J. M. Boothby, H. Kim, M. R. Shankar, T. H. Ware, *ACS Appl. Mater. Interfaces* **2017**, *9*, 37332; b) S. Gantenbein, K. Masania, W. Woigk, J. P. W. Sesseg, T. A. Tervoort, A. R. Studart, *Nature* **2018**, *561*, 226; c) A. Kotikian, R. L. Truby, J. W. Boley, T. J. White, J. A. Lewis, *Adv. Mater.* **2018**, *30*, 1706164; d) D. J. Roach, X. Kuang, C. Yuan, K. J. Chen, H. J. Qi, *Smart Mater. Struct.* **2018**, *27*, 125011; e) A. Kotikian, C. McMahan, E. C. Davidson, J. M. Muhammad, R. D. Weeks, C. Daraio, J. A. Lewis, *Sci. Rob.* **2019**, *4*, eaax7044; f) M. O. Saed, C. P. Ambulo,

H. Kim, R. De, V. Raval, K. Searles, D. A. Siddiqui, J. M. O. Cue, M. C. Stefan, M. R. Shankar, T. H. Ware, *Adv. Funct. Mater.* **2019**, *29*, 1806412; g) C. Zhang, X. L. Lu, G. X. Fei, Z. H. Wang, H. S. Xia, Y. Zhao, *ACS Appl. Mater. Interfaces* **2019**, *11*, 44774.

[22] X. Peng, X. Kuang, D. J. Roach, Y. Wang, C. M. Hamel, C. Lu, H. J. Qi, *Addit. Manuf.* **2021**, *40*, 101911.

[23] L. Ren, B. Li, Y. He, Z. Song, X. Zhou, Q. Liu, L. Ren, *ACS Appl. Mater. Interfaces* **2020**, *12*, 15562.

[24] a) N. A. Traugutt, D. Mistry, C. Luo, K. Yu, Q. Ge, C. M. Yakacki, *Adv. Mater.* **2020**, *32*, 2000797; b) S. Y. Jeon, B. Shen, N. A. Traugutt, Z. Zhu, L. Fang, C. M. Yakacki, T. D. Nguyen, S. H. Kang, *Adv. Mater.* **2022**, *34*, 2200272.

[25] M. A. Skylar-Scott, S. Gunasekaran, J. A. Lewis, *Proc. Natl. Acad. Sci. USA* **2016**, *113*, 6137.

[26] J. Zhu, Q. Zhang, T. Yang, Y. Liu, R. Liu, *Nat. Commun.* **2020**, *11*, 3462.

[27] X. He, Y. Ding, Z. Lei, S. Welch, W. Zhang, M. Dunn, K. Yu, *Addit. Manuf.* **2021**, *40*, 101921.

[28] A. De Marzi, G. Giometti, J. Erler, P. Colombo, G. Franchin, *Addit. Manuf.* **2022**, *54*, 102727.

[29] a) S. C. Ligon, B. Husár, H. Wutzel, R. Holman, R. Liska, *Chem. Rev.* **2014**, *114*, 557; b) Z. Zhao, X. Mu, J. Wu, H. J. Qi, D. Fang, *Extreme Mech. Lett.* **2016**, *9*, 108.

[30] a) L. del-Mazo-Barbara, M.-P. Ginebra, *J. Eur. Ceram. Soc.* **2021**, *41*, 18; b) J. Kutin, I. Bajsić, *J. Fluids Struct.* **2014**, *50*, 171.

[31] a) K. Liu, J. Wu, G. H. Paulino, H. J. Qi, *Sci. Rep.* **2017**, *7*, 3511; b) H. Lee, Y. Jang, J. K. Choe, S. Lee, H. Song, J. P. Lee, N. Lone, J. Kim, *Sci. Rob.* **2020**, *5*, eaay9024; c) Z. Wang, K. Li, Q. He, S. Cai, *Adv. Mater.* **2019**, *31*, 1806849.

[32] S. Wu, L. Yue, Y. Jin, X. Sun, C. Zemelka, H. J. Qi, R. Zhao, *Adv. Intell. Syst.* **2021**, *3*, 2100107.